



Hybrid Energy Flotation™ — on the optimization of fine and coarse particle kinetics in a single row

by D. Govender*, D. Lelinski*, and F. Traczyk*

Synopsis

Theoretical flotation models suggest that there is a positive relationship between bubble-particle collision rates and turbulent kinetic energy dissipation. Fine particle flotation performance is generally enhanced by increased collision frequency and hence higher energy dissipation. Contrarily, increased turbulence in the rotor-stator region is related to higher detachment frequency of the coarser size range. Therefore, the optimal modes of recovery for the 'fine' and 'coarse' size classes appear to be diametrically opposed.

Industrial applications have previously confirmed that applying greater power to flotation slurries yields significant improvements in fine particle recovery. However, recovery of the coarser size class favours a different flotation environment. An improvement in the flotation kinetics of the fine and coarse size classes, provided there is no adverse metallurgical influence on the intermediate size ranges, is obviously beneficial to the overall recovery response. Managing the local turbulent kinetic energy dissipation, and hence the power imparted to the slurry, offers the benefit of targeting the particle size ranges exhibiting slower kinetics.

FLSmidth recently introduced the practical implementation of this concept. In principle, it decouples flotation regimes where fine and coarse particles exhibit preferentially recovery. In the case of naturally aspirated machines (Wemco®), it is referred to as Hybrid Energy Flotation™ and incorporates at least three phases:

- ▶ Standard flotation machines (standard energy input, rotor speed (r/min), rotor size/type) at the beginning of the row, where flotation is typically froth-phase limited and operational and set-up parameters have a limited influence on the recovery
- ▶ Higher-powered flotation machines (high rotor speed, high-power rotor size/type) at the end of the row to improve fine particle recovery
- ▶ Lower-powered flotation machines (low rotor speed, low power rotor size/type) to enhance coarse particle recovery.

A CFD-based flotation model is used to highlight the effect of turbulent dissipation energy on attachment and detachment rates. Preferential collection zones for 'fine' and 'coarse' particles are predicted for both forced-air and naturally aspirated machines. The greater predominance of UG2 ore types, coupled with the skewed feed distribution of platinum group metals (PGMs) to the finer size fractions, suggests that PGM flotation circuits are not designed for optimal recovery across the size distribution. The application of the hybrid energy concept to PGM flotation offers a possible shift towards a more efficient flotation circuit solution through a managed distribution of energy.

Keywords

CFD-based model, attachment, detachment, energy dissipation, Hybrid Energy Flotation™, forced air, naturally aspirated.

Introduction

Operation of the Wemco® flotation machine

The Wemco unit is a naturally-aspirated mechanical flotation machine. Air is induced via a standpipe and an inlet pipe open to the atmosphere. For Wemco flotation machines of constant rotor diameter, hydrodynamic parameters are defined as the relationship between air ingestion and primary liquid circulation as functions of rotor submergence, rotor engagement, and rotor speed. In turn, rotor submergence is defined as the vertical distance from the top of the rotor to the froth-pulp interface, and rotor engagement as the vertical distance that the rotor is encased within the draft tube. At constant rotor submergence, an increase in rotor speed results in an increase in aeration (or superficial gas velocity), and specific power. At constant submergence and rotor speed, liquid circulation varies almost linearly with rotor engagement. At constant rotor speed, an increase in rotor submergence results in a decrease in air induction, with a simultaneous increase in the draft tube liquid circulation (the latter being synonymous with absorbed power and often manifested as specific power input). The rotor-disperser combination serves the same purpose as a rotor-stator arrangement in a forced-air machine.

Operation of the Dorr-Oliver® flotation machine

The Dorr-Oliver machine utilizes a forced-air mechanism to perform the dual functions of air dispersion and solids suspension. Air is introduced into the tank via an external

* FLSmidth Salt Lake City Inc.

© The Southern African Institute of Mining and Metallurgy, 2013. ISSN 2225-6253. This paper was first presented at the 5th International Platinum Conference 2012, 18–20 September 2012, Sun City, South Africa.

Hybrid Energy Flotation™ — on the optimization of fine and coarse particle kinetics

blower. Air is supplied to the centre of the rotor down the rotating hollow shaft that suspends and rotates the rotor. The stator serves to prevent swirling of the slurry, which would otherwise inhibit good separation of the recovered minerals. The stator also contributes to fine bubble generation and particle-bubble contact. Furthermore, the Dorr-Oliver design promotes recirculation of unrecovered minerals by containing and defining the intense mixing zone in the bottom of the tank. The aeration rate and rotor speed are invariably correlated to the slurry circulation and absorbed power. The sensitivity of liquid circulation and power to rotor speed decreases with an increase in aeration rate. The rotor cavities experience progressive air volume increases, and pumping performance is gradually reduced.

CFD-based flotation models

The utilization of computational fluid dynamics (CFD) in flotation machine design has gained prominence over the past decade. Figure 1 illustrates the rotor-stator domain of interest in relation to the assembly of the Wemco and Dorr Oliver flotation machines. Ragab *et al.* (2012) use the Euler-Euler two-fluid model in their multiphase flow simulation of the Wemco 0.8 m³ machine. Mono-sized bubble diameters of 1.0, 0.7, and 0.5 mm are assumed. Ragab *et al.* also specified a new boundary condition to allow air to enter and exit the machine. This is analogous to a ‘breathing’ machine, and contrasts with the steady-state airflow approach used in the CFD evaluation of forced-air machines. The Dorr-Oliver 6 m³ simulation utilizes a steady airflow rate of 2.63 m³/min. Mono-sized bubble diameters of 2.0, 1.0, and 0.5 mm are assumed. The Schiller-Naumann drag model and Shear Stress Transport turbulence model complement the simulation (Ragab *et al.*, 2012).

The effect of turbulent kinetic energy dissipation has long been incorporated into theoretical flotation models. The first-principle flotation models developed by Ragab *et al.* (2012) address the effect of energy dissipation on pulp recovery, and

thus its effect on machine design. Ragab *et al.* describe two rate constants, an attachment and detachment constant, each contingent upon the probabilities of collision, adhesion, and stabilization. The practical implementation of the CFD model outputs on large industrial cells is discussed later.

Attachment model

The flotation rate attachment constant k_{att} [m³/s] may be defined as:

$$k_{att} = Z_{pb,1} P_c P_a P_s \quad [1]$$

where the individual probabilities of the sub-processes of bubble-particle collision, attachment, and stabilization are represented by P_c , P_a , and P_s , respectively. The bubble-particle collision frequency (number of collisions per unit time and unit volume) may be represented by $Z_{pb,1}$ [m³/s] (Ragab *et al.*, 2012)

Abrahamson’s (1975) collision frequency accelerative mechanism may be used to model the bubble-particle collision frequency $Z_{pb,1}$:

$$Z_{pb,1} = 2^{2/3} \pi^{1/2} N_p N_b d_{pb}^2 \sqrt{(U_p^2 + U_b^2)} \quad [2]$$

where N_p and N_b are the number of particles and bubbles per unit volume, d_{pb} is the average collision diameter of bubble and particle [m], and U_p and U_b are the turbulent root-mean-square (RMS) velocities of particle and bubble [m/s], respectively.

The Abrahamson (1975) model may be re-written as Equation [3] (Schubert and Bischofberger, 1978; Ragab *et al.*, 2012), with the turbulent RMS velocities represented by Equation [4] (Liepe and Möckel, 1976; Ragab *et al.*, 2012).

$$z_{pb,1} = 5 \left(\frac{d_p + d_b}{2} \right)^2 (U_p^2 + U_b^2)^{1/2} \quad [3]$$

where d_p and d_b are the respective diameters of the particles and bubbles [m].

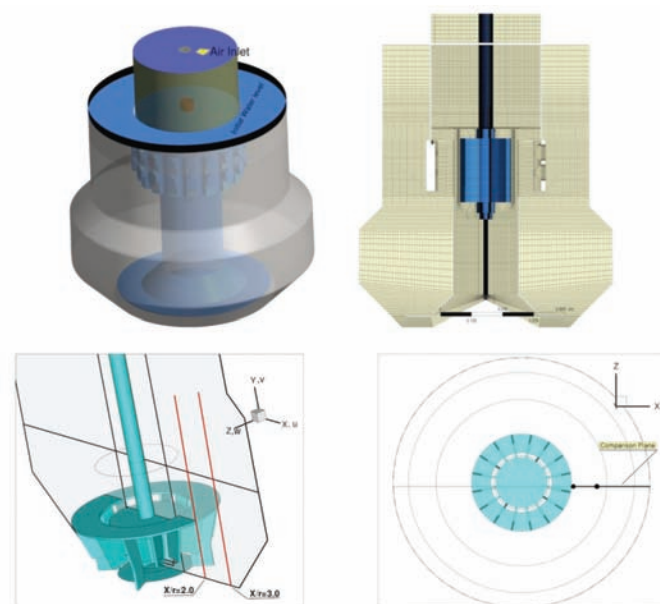


Figure 1—Wemco® mechanism assembly (top left) and mesh grid (top right). Dorr-Oliver domain of interest (bottom left and right)

Hybrid Energy Flotation™ — on the optimization of fine and coarse particle kinetics

$$U_i = \frac{0.4 \epsilon^{4/9} d_i^{7/9}}{\nu^{1/3}} \left(\frac{|\rho_p - \rho_f|}{\rho_f} \right)^{2/3} \quad [4]$$

where ϵ is the dissipation rate of the turbulent kinetic energy per unit mass [W/kg], ν is the kinematic viscosity of the fluid [m²/s], ρ_f is the fluid density [kg/m³], ρ_p is the particle density [kg/m³] and d_i is the particle diameter [m]. The probability of bubble-particle collision is represented by (Yoon and Luttrell, 1989; Koh and Schwarz, 2006; Ragab *et al.*, 2012):

$$P_c = \left(\frac{3}{2} + \frac{4}{15} \text{Re}_b^{0.72} \right) \frac{d_p^2}{d_b^2} \quad [5]$$

where the bubble Reynolds number is defined by $\text{Re}_b = d_b U_b / \nu$. The probability of adhesion may be expressed as Equation [6] (Yoon and Luttrell, 1989; Koh and Schwarz, 2006; Ragab *et al.*, 2012):

$$P_a = \sin^2 \left(2 \tan^{-1} \exp \left[\frac{-(45 + 8 \text{Re}_b^{0.72}) U_b t_{ind}}{15 d_b (d_b / d_p + 1)} \right] \right) \quad [6]$$

where $t_{ind} = \frac{75}{\theta} d_p^{0.6}$ (Koh and Smith, 2011; Ragab *et al.*, 2012; Dai *et al.*, 1999) is the induction time [s] and θ = the bubble-particle contact angle [degrees]. Induction time may be defined as the time required for liquid film thinning and drainage to occur between a hydrophobic particle and air bubble (Koh and Smith, 2011).

Ragab *et al.* (2012) utilize the modified Schulze (1993) expression (Bloom and Heindel, 2003) to evaluate the stabilization probability:

$$P_s = 1 - \exp \left(A_s \left[1 - \frac{1}{\min(1, Bo^*)} \right] \right) \quad [7]$$

where Bo^* is the modified Bond number defined by Equation [8] (Koh and Schwarz, 2006; Ragab *et al.*, 2012) as:

$$Bo^* = \frac{d_p^2 \left[\Delta \rho g + 1.9 \rho_p \epsilon^{2/3} (d_p / 2 + d_b / 2)^{-1/3} \right] + 1.5 d_p (4 \sigma / d_b - d_b \rho g) \sin^2(\pi - \theta / 2)}{6 \sigma \sin(\pi - \theta / 2) \sin(\pi + \theta / 2)} \quad [8]$$

where $A_s = 0.5$ (Bloom and Heindel, 2003), σ is the surface tension [N/m], $\Delta \rho = \rho_p - \rho_f$, and g is the gravitational constant [m/s²].

Detachment model

The bubble-particle detachment rate constant k_{det} [s⁻¹] may be defined by Equation [9] (Koh and Schwarz, 2006; Ragab *et al.*, 2012):

$$k_{det} = Z_{pb,2} P_d = Z_{pb,2} (1 - P_s) \quad [9]$$

where $Z_{pb,2}$ is the detachment frequency [s⁻¹], P_d is the probability of detachment, and has an assumed equivalence to $1 - P_s$. (Bloom and Heindel, 2003; Ragab *et al.*, 2012) define the detachment frequency as:

$$Z_{pb,2} = \frac{\sqrt{C_1 \epsilon^{1/3}}}{(d_p + d_b)^{2/3}} \quad [10]$$

where $C_1 = 2$ is an empirical constant.

CFD-based pulp recovery rate

In Figure 2 the effects of particle diameter (d_p), particle specific gravity (γ_p), contact angle (θ), and surface tension (σ) on the recovery rate constant were evaluated in a Wemco two-phase CFD-based model developed by Ragab *et al.*, (2012).

The attachment and detachment models presented here indicate that both these sub-processes are affected by the turbulent energy dissipation rate. Therefore, the net attachment rate will be contingent upon the energy dissipation rate management. Schubert (1989, 2008) defines the mean energy dissipation rate $\bar{\epsilon}$ as the ratio of the total specific power input M [W] to the overall slurry mass [kg] (Equation [11]).

$$\bar{\epsilon} = \frac{P}{M} \quad [11]$$

This macro relationship assumes consistent hydrodynamic conditions throughout the cell. A multiplier may be used to relate the local rotor-disperser power input to that of the total slurry mass, but with no spatial distribution of the energy dissipation rate, the effect of hydrodynamics on the local net attachment rate and kinetic rate is unknown (Schubert, 2008; Ragab *et al.*, 2012). Deglon (2005) and Grano (2005) also suggest the need for an optimum power input to mechanically agitated flotation machines. The Wemco 0.8 m³ CFD-based model yields the local recovery rate

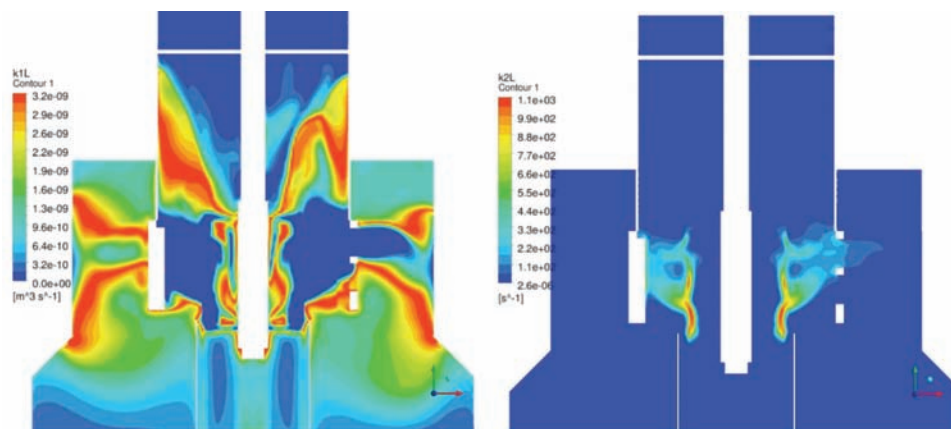


Figure 2—Wemco local attachment (left) and detachment (right) rates for $d_p = 100 \mu\text{m}$; $\gamma_p = 4.1$; $\theta = 40^\circ$; $\sigma = 0.06 \frac{\text{N}}{\text{m}}$; $d_b = 0.7 \text{ mm}$

Hybrid Energy Flotation™ — on the optimization of fine and coarse particle kinetics

constant as one of the outputs, and may therefore be used both as a process optimization and flotation machine design tool (Ragab *et al.*, 2012).

Understanding the interaction between particle diameter, local energy dissipation rate, contact angle, and local air fraction on local attachment rates is integral to flotation machine design, setup, and operation. Ragab *et al.* (2012) define the average pseudo pulp recovery rate k_{1a}^* in Equation [12]:

$$k_{1a}^* = \frac{R_f}{V} \int k_1^* (1 - \beta) dV \quad [12]$$

where $R_f = 1$ is the froth recovery factor and $\beta = 0$. Koh and Schwarz (2006) define β as a bubble loading parameter where $\beta = 1$ for fully loaded bubbles and $\beta = 0$ for clean bubbles. The recovery rate constant k_1^* is defined as:

$$k_1^* = \frac{k_{att} \alpha (1 - \alpha)}{v_b} \quad [13]$$

where α and v_b represent the air volume fraction and bubble volume m^3 , respectively. The Wemco pulp recovery rate constant k_1^* is illustrated in Figure 3 for the 0.7 mm bubble diameter as a function of the particle diameter in a vertical mid-plane. The 10 μm particles show a higher recovery rate within the energy-intensive rotor-disperser mixing zone. Recovery rates for this particle size class peter out in the less turbulent region outside the disperser. The CFD output for the 200 μm size fraction suggests an opposing attachment

regime. The region external to the disperser is of a more quiescent nature and preferential collection is localized here. The positive net attachment rate of the fine particle sizes within the rotor-disperser region is dependent on the higher local energy dissipation rates in the vicinity of the impeller blade tip. Contrastingly, coarse particle positive net attachment rates result from the low dissipation regions at the disperser periphery. Additionally, the average pseudo pulp recovery rate k_{1a}^* is a function of the selected parameters (illustrated in Figure 4). Similar trends are shown for the production and dissipation of energy quantities in Figure 5 and Figure 6 for the Dorr-Oliver mechanism.

Industrial experimentation

In a single flotation row, the complexity of the physico-chemical process generally yields a distribution of flotation pulp kinetic values. Comparatively, typical flotation row design will incorporate a consistent power input per flotation row or duty.

Standardization and machine spares commonality are drivers here. Required power input may vary between flotation applications (and duties), but is typically minimized after the just-suspended solids criterion has been achieved (Schubert, 2008). In the case of a self-aspirated machine, additional hydrodynamic constraints may apply.

Unless the flotation feed particle size distribution is inherently fine, the incremental increase of collision frequency on unsized feed may offer no potential benefit.

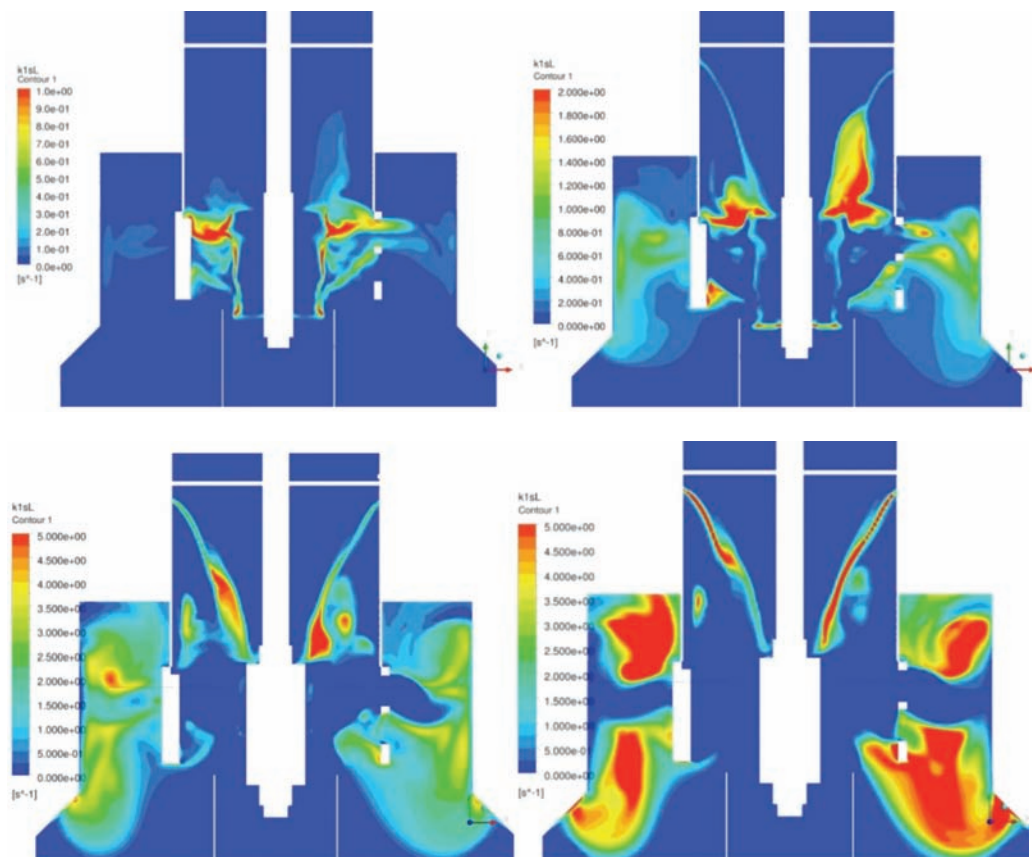


Figure 3—Wemco pulp recovery rate k_1^* for 0.7 mm bubble diameter as a function of particle size $d_p = 10 \mu m$ (top left), $d_p = 40 \mu m$ (top right), $d_p = 100 \mu m$ (bottom left), $d_p = 200 \mu m$ (bottom right)

Hybrid Energy Flotation™ — on the optimization of fine and coarse particle kinetics

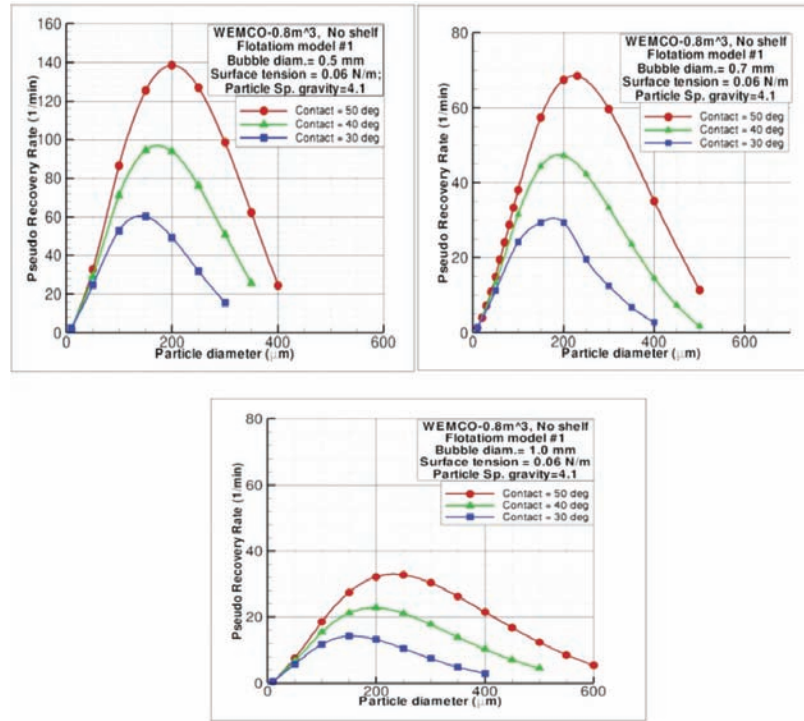


Figure 4—Wemco average pulp flotation rate $k_{1,q}$ as a function of contact angle and bubble size (0.5 mm (top left), 0.7 mm (top right), and 1.0 mm (bottom))

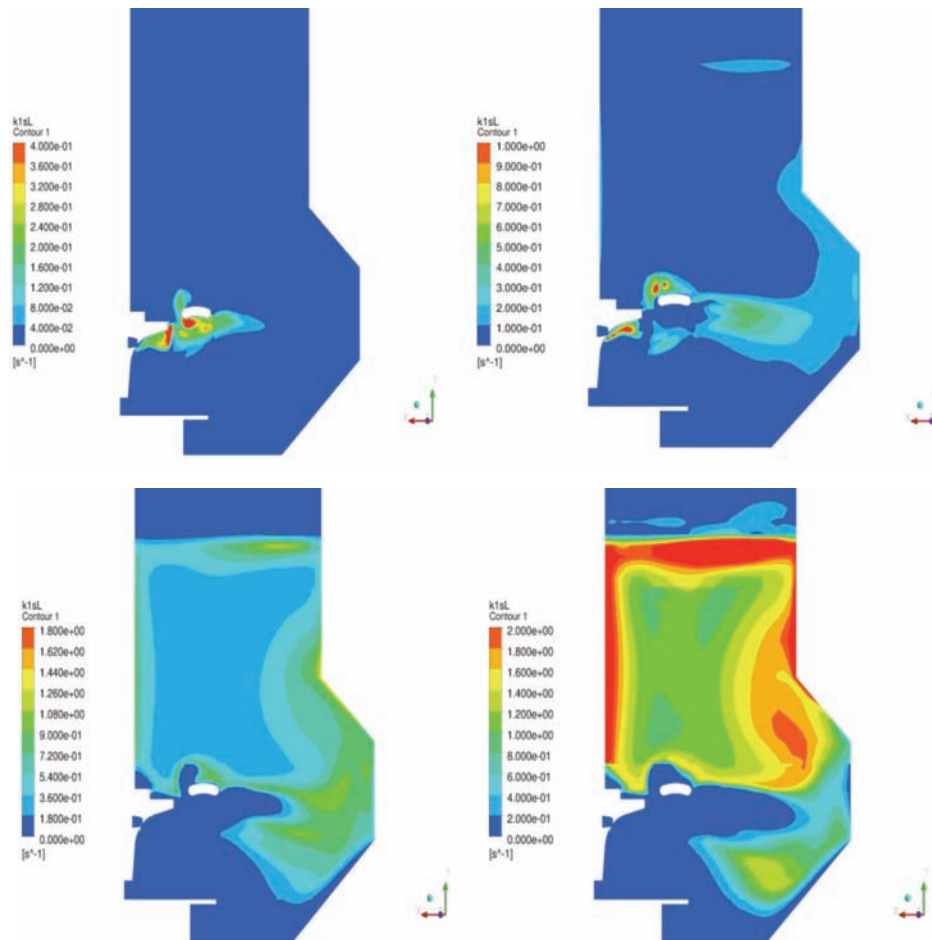


Figure 5—Dorr-Oliver pulp recovery rate k_1 for 1.0 mm bubble diameter as a function of particle size $d_p = 10 \mu\text{m}$ (top left), $d_p = 40 \mu\text{m}$ (top right), $d_p = 100 \mu\text{m}$ (bottom left), $d_p = 200 \mu\text{m}$ (bottom right)

Hybrid Energy Flotation™ — on the optimization of fine and coarse particle kinetics

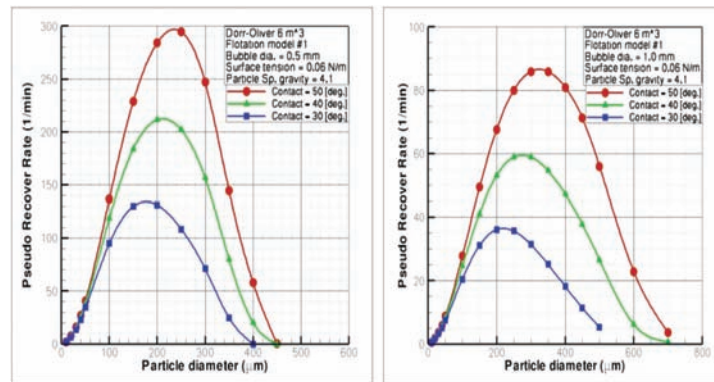


Figure 6—Dorr-Oliver average pulp flotation rate k_{1d} as a function of contact angle and bubble size (0.5 mm (left) and 1.0 mm (right))

Grano (2006) and Deglon (1998) have shown that the recovery in the coarse size range is typically negated by the increase in turbulent energy dissipation.

Coarse particle recovery tends to be inhibited by the predominance of turbulence in a mechanical flotation cell (Jameson, 2010), possible surface tension effects (Sherrell and Yoon, 2005) and the froth recovery component. Schubert (2008) suggests that pre-classification of the flotation feed into fine and coarse streams offers independent treatment of the size fractions. Power (or machine hydrodynamics) should be individually optimized to maintain solids suspension in the coarse stream, and maximize collision frequency in its finer counterpart (Schubert, 2008). However, Ata *et al.* (2012) contend that the presence of fines provides the necessary froth stability to propagate coarse particle recovery. Therefore, turbulence management of an unclassified feed in a single row may be the preferred method of implementation.

The application of turbulent dissipation energy management manifests itself in the Hybrid Energy Flotation™ technology specific to the distribution of valuable minerals in the flotation feed. CFD-based models suggest that inherently fine distributions should benefit from higher power inputs. Valuable mineral distributions skewed toward the coarser range favour a lower rate of energy dissipation. In general, recovery-by-size distributions are more normal in nature. Therefore, valuable mineral recovery resulting from a distribution of power input within a single row appears to offer a metallurgical design of greater specificity. This strategy also suggests a shift away from the old orthodoxy of a residence time-constrained flotation row to a customized turbulence-distribution metallurgical design. The application of the Hybrid Energy Flotation™ technology in bulk copper-molybdenite flotation duties is now discussed.

Results and discussion

Case one

The first case study involves a porphyry copper rougher-scavenger row comprising 5 × 257 m³ Wemco machines. Each machine was initially equipped with standard installed power and operated at standard rotor speeds. An atypical difference between laboratory and full-scale molybdenite recoveries evolved into a simple laboratory-scale investigation into the

effect of bulk turbulent dissipation energy on molybdenite recovery. An initial liquid residence time distribution evaluation of the five-cell row yielded no signs of short-circuiting (Figure 7).

The ratio of experimental to theoretical residence times ranged from 1.01 to 1.10 (Govender, 2010). A typical ratio of 1±0.1 is indicative of well-mixed vessels. The curve shape, characterized by the absence of an early, sharp peak is indicative of no short-circuiting. Additionally, the lack of a long, drawn-out tails section typifies a mixing vessel devoid of stagnant or dead volume (Govender, 2010). Thereafter, site personnel tested the effect of additional residence time by temporarily converting existing 8.5 m³ cleaner cells into scavenger duty units. The scavenger tails process stream was then re-routed to these machines to evaluate the effect of the additional residence time on unsized recovery. Table I highlights the measured scavenger-stage recovery response. The associated recovery variance is typical of scavenger duty industrial-scale evaluations. Figure 8 also suggested that the molybdenite recovery rate was tied to the residence time. The

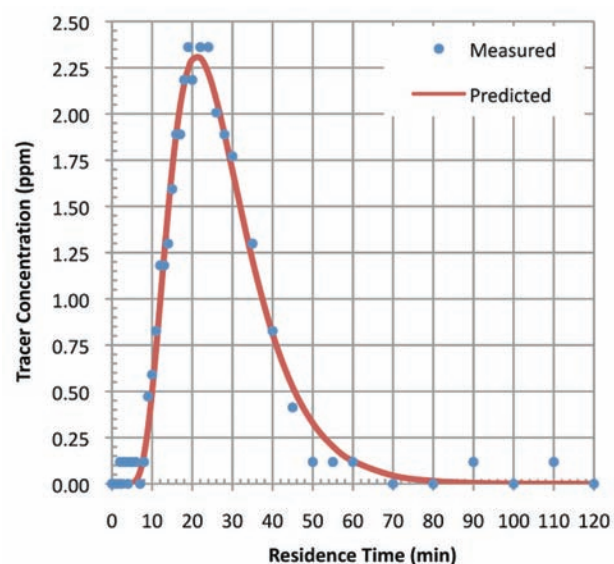


Figure 7—Liquid tracer test residence time distribution (measured vs. fitted)

Hybrid Energy Flotation™ — on the optimization of fine and coarse particle kinetics

correlation coefficient between the throughput and recovery datasets is -0.64, indicating a fairly strong inverse relationship.

The flotation rate of molybdenite in porphyry copper applications, which often lags that of copper (Zanin *et al.*, 2009), has been shown to improve significantly with increased specific power input. Molybdenite flotation kinetics, and its response to power input, may be attributed to the platelet shape of molybdenite particles produced via specific fragmentation mechanisms (Zanin *et al.*, 2009). The resulting shape factor may result in a flotation rate response that is more amenable to increased collision frequency (Zanin *et al.*, 2009). The response to collision frequency is therefore similar to that theorized for fine particle flotation.

Schubert (2008) concludes that collision frequency is positively correlated to the energy dissipation rate (ϵ_R) in the rotor-stator region, while exhibiting an inverse relationship to the fluid viscosity (ν). Consequentially, Schubert maintains that a maximal ϵ_R/ν ratio is beneficial to fine particle flotation.

Figure 9 illustrates the size-by-size distribution of the monthly tailings composites. Both copper and molybdenite losses are visibly skewed towards the fine fraction. Utilizing a laboratory-scale randomized-block 2^2 factorial experiment design, the effect of feed slurry density on molybdenite and copper recovery is presented in Figure 10. The randomized test runs and two-level factorial design set-points are summarized in Table II. Each of the test samples was sub-sampled from a composite feed sample. The solids concentration target was achieved by concentration or process water

dilution of the primary feed. Rotor speed was confirmed with a tachometer. The qualitative slurry density scale is represented by two factor levels: 'low' = 24 wt% and 'high' = 35 wt% feed solids concentration. The effect of rotor speed only was not significant at the 95 per cent confidence limit, and therefore the average value is utilized in the solids concentration evaluation. Overall molybdenite recovery increased markedly with the 11 per cent absolute decrease in solids concentration, and the effect is statistically significant.

Copper recovery illustrates a contradictory relationship but, statistically, no effect is observed due to the overlapping of the confidence bands at the high and low density levels. It is still probable that the net copper attachment rate was adversely affected with the increase in turbulent energy dissipation.

In a similar evaluation, Zanin *et al.* (2009) noticed an inverse correlation between molybdenite recovery and feed solids concentration. This was attributed partially to the

Table I

Effect of additional residence time on scavenger stage recovery

Species	No. of samples	Additional recovery (%)	
		Average (%)	Standard deviation (%)
Cu	6	14.6	13.2
Mo	6	12.9	9.1

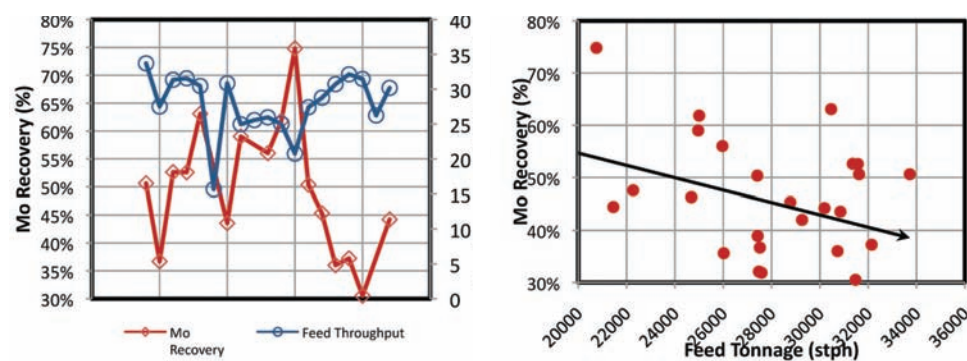


Figure 8—Effect of residence time on molybdenite recovery (daily averages)

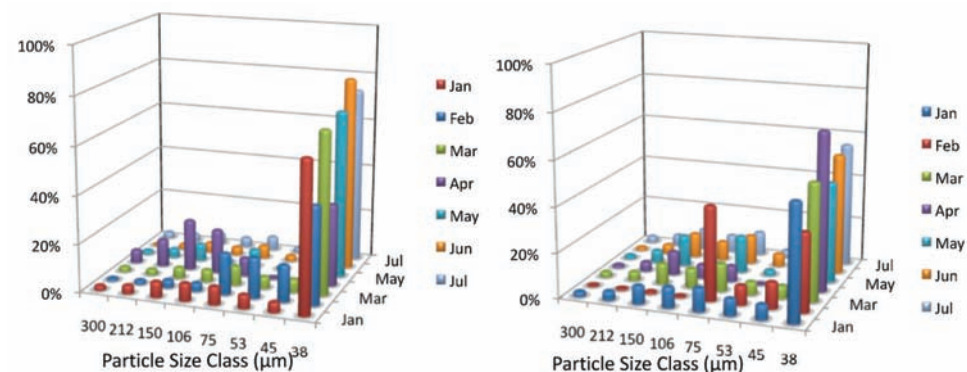


Figure 9—Size-by-size distribution of Cu (left) and MoS₂ (right) in rougher-scavenger tails

Hybrid Energy Flotation™ — on the optimization of fine and coarse particle kinetics

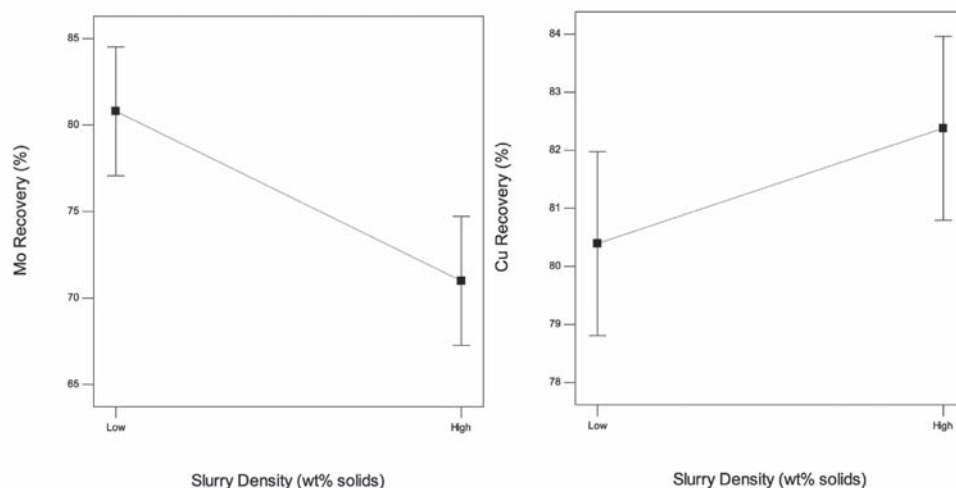


Figure 10—Effect of solids concentration on MoS₂ (left) and Cu (right) recovery

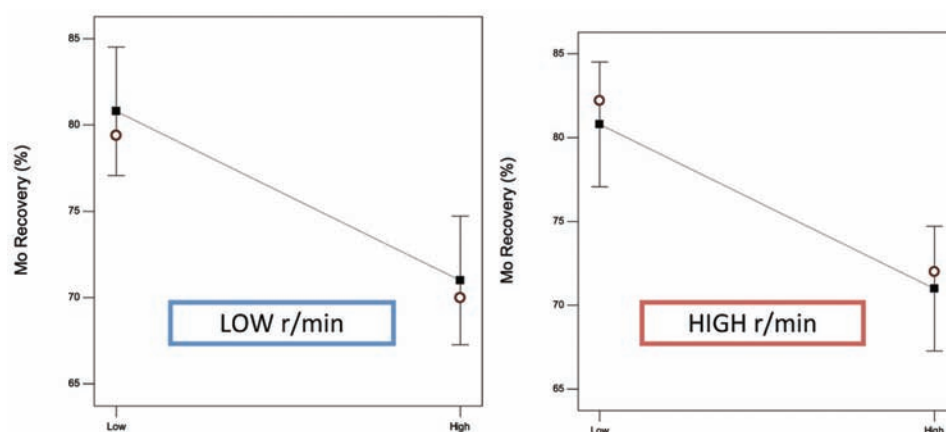


Figure 11—Laboratory-scale MoS₂ recovery response to the feed solids concentration and rotor speed interaction. The circular design data points represent the low rotor speed condition (left), and are compared to the high rotor speed condition (right)

Test ID	Rotor speed (r/min)	Solids concentration (%w/w)
S13	1455 (H)	24 (L)
S14	1200 (L)	24 (L)
S15	1200 (L)	35 (H)
S16	1455 (H)	35 (H)

increased collision frequency borne out of the reduction in fluid viscosity. In Figure 11 MoS₂ recovery is plotted as a function of the interaction of rotor speed *and* viscosity (inferred from solids concentration). At low rotor speed design levels, the recovery response lags the average; the opposite relationship applies at the high rotor speed level. Therefore, in manipulating the macro turbulent local energy dissipation rate and/or slurry viscosity, the net attachment rate increased. Consequentially, a positive response in MoS₂ overall recovery was observed.

The effect of increased turbulence on the concentrate grade response was also evaluated on a laboratory-scale basis (Figure 12). Low-level solids feed concentrations have distinct gangue entrainment reduction benefits. This data subset *visually* indicates a superior grade-recovery curve at the high-level rotor speed condition.

Upon confirmation of the energy dissipation-recovery effect, the penultimate cell in the five-cell rougher-scavenger row was enabled with a larger installed motor capacity, and the specific power input increased via a variable-frequency drive (actual plant feed could not be diluted due to process water constraints). Froth depth was simultaneously increased to negate gangue entrainment. The increase in rotor speed was constrained by the installed motor power, but molybdenite row recovery showed no optimum in the tested rotor speed range i.e. there was no indication of a decrease in the net attachment rate with an increase in power input. Figure 13 illustrates the recovery responses of the plant-scale trial. Stage recoveries (on a relative basis) illustrate a loose, positive response to power input. The final two cells in the rougher-scavenger row were then changed to a constant, maximum rotor speed operational condition.

Hybrid Energy Flotation™ — on the optimization of fine and coarse particle kinetics

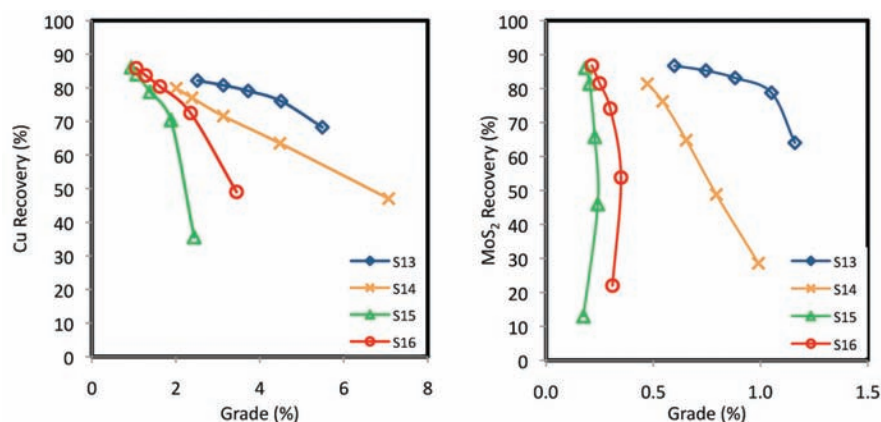


Figure 12—Laboratory-scale Cu (left) and MoS₂ (right) grade-recovery response to the feed solids concentration and rotor speed interaction

Case two

A copper concentrator comprises a Semi Autogenous - Ball Mill - Crushing Circuit (SABC) grinding circuit followed by a bulk beneficiation step. The six rows of Wemco rougher-scavenger cells produce a bulk copper-molybdenite concentrate. The fast-floating rougher concentrate is diverted to rougher-cleaner columns, while the scavenger concentrate is reground. The regrind circuit product is enriched in a series of cleaner-scavenger steps utilizing a combination of column and mechanically-agitated machines. Molybdenite separation from the bulk concentrate occurs in the molybdenite flotation plant. The installation of the Wemco and Dorr-Oliver 300 m³ SuperCell™ flotation machines in cleaner-scavenger mode afforded FLSmidth the opportunity to optimize the flotation machines in terms of hydrodynamics and metallurgy.

Forming part of the metallurgical optimization was a study of the effect of power absorption on copper and molybdenite recoveries.

The relatively dilute feed to the SuperCell™ consisted of the regrind circuit classification overflow product, generally comprising 5–10wt% solids. Figure 14 is indicative of the feed particle size distribution for the first two campaigns of the SuperCell™ evaluation. The d_{80} for both campaigns ranged from 20–30 μm , with a predicted d_{50} of less than 10 μm .

Wemco mechanism

The feed to the Wemco SuperCell™ assayed approximately 10.5% Cu and 1% MoS₂. Herein, the metallurgical performance of the SuperCell™ is evaluated for a constant feed flow rate (734 m³/h). Similarly, the pilot cell volumetric feed rate equates to a stable 11.3 m³/h. The response diagrams that follow are also indicative of these static conditions. Five test campaigns were completed, accommodating mineralogical and reagent variations coupled with general process noise. Experimental design incorporated a full central composite design (CCD) utilizing rotor speed and froth depth as input variables. Each campaign comprised thirteen randomized test runs, with assay-by-size data available for select test runs.

Figure 15 suggests rotor speed as the more significant factor influencing copper recovery. An increase in the SuperCell™ agitator speed from 88 r/min to 98 r/min yielded

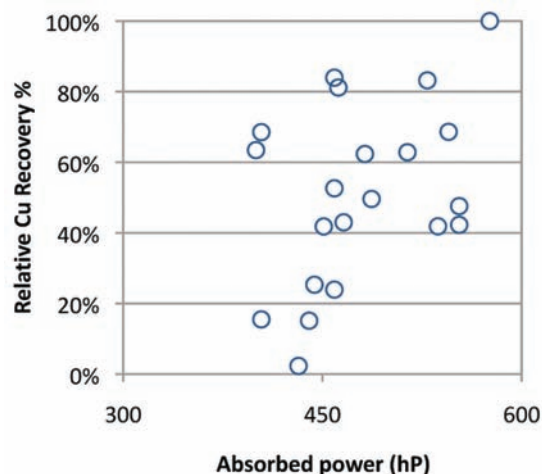


Figure 13—Plant-scale Cu (left) and MoS₂ (right) relative stage recovery responses to power input

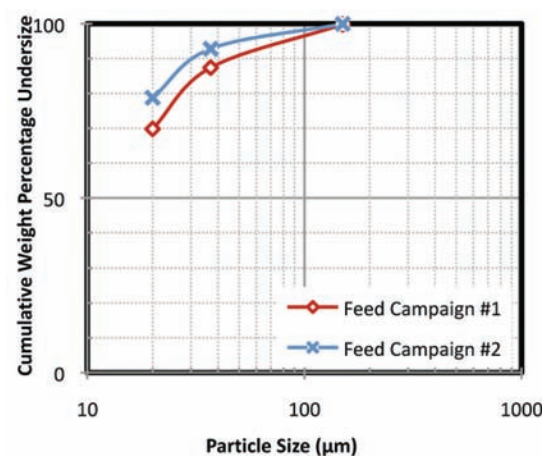


Figure 14—Wemco SuperCell™ semi-log feed particle size distribution

a 9 per cent increase in copper stage recovery. A similar effect is observed for the pilot cell operation. The effect of rotor speed and froth depth on absorbed power (kW) is depicted in Figure 16, with rotor speed predominantly influential on the absorbed power. The slight froth depth effect is explained by

Hybrid Energy Flotation™ — on the optimization of fine and coarse particle kinetics

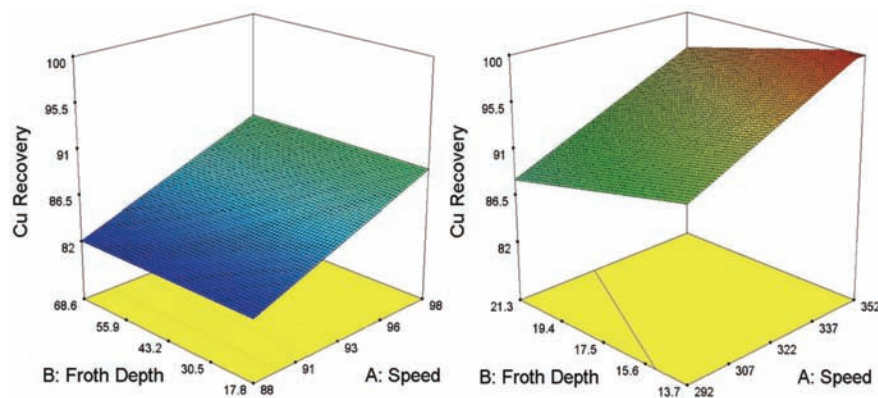


Figure 15—Cu recovery (%) response surface for the Wemco SuperCell™ (left) and the pilot cell (right) developed for the ore type treated in second campaign

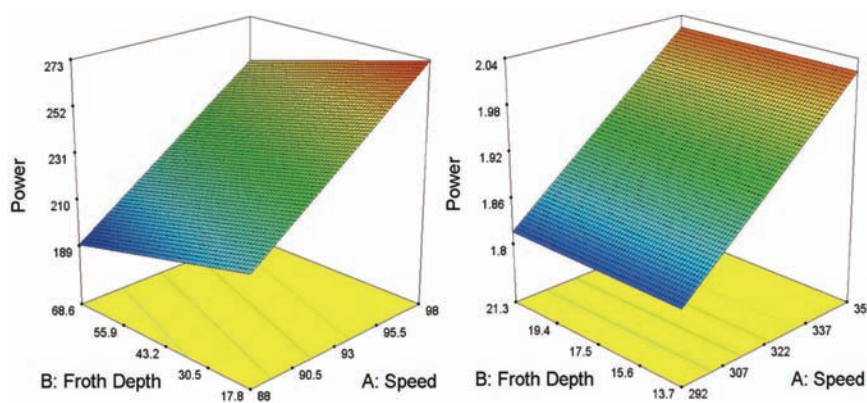


Figure 16—Absorbed power (kW) response surface for the Wemco SuperCell™ (left) and the pilot cell (right)

the apparent change in submergence. The average absorbed power of the SuperCell™ ranged from about 190 kW to 270 kW, translating into a 0.6–0.9 kW/m³ specific power range. Power absorption of the pilot cell ranged from 1.8 kW to 2.0 kW or a 1.2–1.3 kW/m³ specific power range.

Grano (2006), Schubert (2008), and Deglon (1998) report that the effect of power or agitation on recovery on an unsized basis is less likely to be observed, due to fine particle recovery improvements being offset by the decrease in attachment efficiency of the coarser particle size fraction. This is further corroborated by Equation [10]. With a minor contribution from the coarse particle size fraction in the classified regrind mill product, the unsized SuperCell™ feed material could still be construed as fine. But, if the copper and molybdenite sub-20 μm size class recoveries are plotted as a function of the absorbed power (Figure 17), the fine-particle recovery-power relationship becomes visually prominent.

Figure 17 suggests that the fine particle recovery deficit commonly observed in base metals operations may be offset by increasing the impeller speed of mechanically-agitated machines. An additional contributory effect is expected to have been provided by the dilute feed (Schubert, 2008).

The development of statistically significant hydrodynamic and metallurgical models for the Wemco SuperCell™ allowed for the more detailed study of the effect of absorbed power on

metallurgical performance of the cell. Table III shows optimum operational conditions required to maximize copper and molybdenite recoveries at a fixed concentrate grade. For the purpose of this exercise, metallurgical characteristics of the feed were maintained at average conditions (as previously described) and volumetric feed flow input was set to 681 m³/h. With an increase in specific power from 0.74 to 0.84 kW/m³, the tabulated data exhibits an increase in the

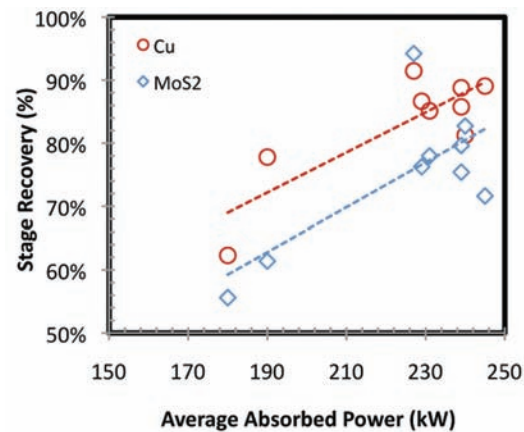


Figure 17—Wemco Cu and MoS₂ recovery of sub-20 μm fraction

Hybrid Energy Flotation™ — on the optimization of fine and coarse particle kinetics

Table III
Summary of metallurgical evaluation

	Specific power (kW/m ³)	Pumping rate (m ³ /min)	Induced airflow (m ³ /min)	Copper grade response (%)	Copper recovery response (%)	Molybdenite recovery response (%)
Scenario 1	0.74	185	35.1	28.0	86.0	82.9
Scenario 2	0.79	187	35.4	28.0	87.5	84.5
Scenario 3	0.84	195	34.0	28.0	88.7	86.0

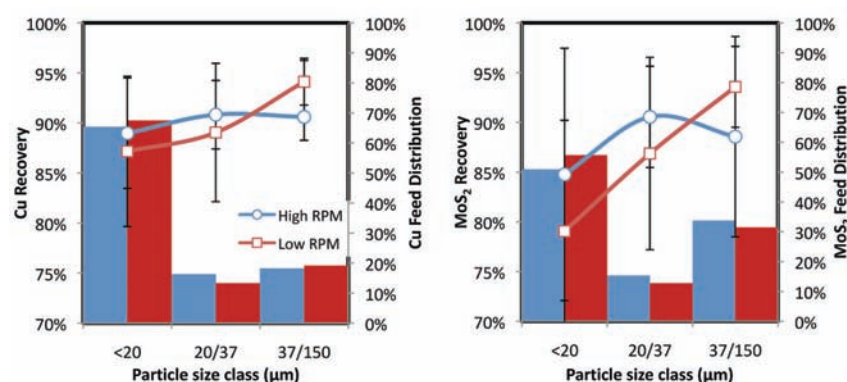


Figure 18—Dorr-Oliver Cu (left) and MoS₂ (right) recovery as a function of particle size and impeller speed. Average feed distribution is compared on the bar chart (secondary axis)

Table IV
Dorr-Oliver CCD experimental design data subset

No. of observations	Rotor speed (r/min)	Mean absorbed power (kW)	Standard deviation - power (kW)	Mean - airflow (m ³ /min)	Standard deviation - airflow (m ³ /min)	Mean - froth depth (inch)	Standard deviation - froth depth (inch)
4	69	86	4	39	8.1	17.1	10.3
7	82	133	10	40.7	4.1	21.9	8.5

expected copper and molybdenite recovery responses of 2.7 per cent and 3.1 per cent, respectively. The recovery responses are constrained by a minimum copper concentrate grade requirement (28 per cent). The improvement in metallurgical performance cannot be explained by an improved higher air flow number as the value of this variable remains fairly constant. Thus, presented data strongly supports the energy dissipation response shown in the CFD model outputs.

Dorr-Oliver mechanism

The Dorr-Oliver mechanism was subject to a similar multi-campaign CCD experimental design. The experimental factors included rotor speed, froth depth, and air flow as input variables. Each campaign comprised twenty-one randomized test runs, with assay-by-size data available for select test runs. Figure 18 compares copper and molybdenite recovery responses as a function of size-by-size recovery and impeller rotational speed. This dataset forms a subset of the overall experimental design evaluation, and relates the recovery response to the impeller speed effect (Table IV).

Figure 18 corroborates the expected responses from the Dorr-Oliver CFD-based model, although there is no statistical significance in the differences between the two rotor speed settings. The lack of significance stems from utilizing a data subset that covers a wide range of operational conditions over multiple campaigns. The solution lies in running a dedicated randomized-block experiment to improve the sensitivity of the rotor speed effect. This suggestion is predicated upon the assumption that test runs made closer together are likely to be of greater similitude than runs made further apart.

Conclusions

Theoretical flotation models indicate that both the attachment and detachment sub-processes are affected by turbulent dissipation energy. The multiphase CFD model developed by Ragab *et al.* (2012) utilizes local turbulent energy dissipation and gas hold-up values, in conjunction with particle, specific gravity, liquid surface tension, and contact angle parameters to estimate the local pulp recovery rate. The CFD models indicate that preferential pulp collection zones in the Wemco and Dorr-Oliver flotation machines may vary with size class

Hybrid Energy Flotation™ — on the optimization of fine and coarse particle kinetics

due to the local turbulent kinetic energy dissipation. The model responses also suggest that the attachment rate of the fine fraction increases in the high-energy zones shrouded by the stator/disperser and adjacent to the impeller tip. While it appears that fine particle flotation kinetics was enhanced with increasing energy dissipation, it is surmised that coarse particle recovery is affected by the detachment sub-process, as induced by the adverse susceptibility to increased fluid turbulence. Coarse particle flotation was therefore favoured in regions of lower energy dissipation.

The flotation rate of molybdenite in porphyry copper applications, which often lags that of copper (Zanin *et al.*, 2009), has been shown to improve significantly with increased specific power input. Molybdenite flotation kinetics, and its response to power input, may be attributed to the platelet shape of molybdenite particles produced via specific fragmentation mechanisms (Zanin *et al.*, 2009). The resulting shape factor may result in a flotation rate response that is more amenable to increased collision frequency. This result was replicated on a laboratory scale for rougher feed. Statistically, copper recovery showed no effect.

The metallurgical evaluation of the 300 m³ Wemco and Dorr-Oliver mechanisms suggested that preferential collection of fine and coarse particles could be achieved by appropriate management of the local turbulent dissipation energy. Proper experimental design is recommended to achieve greater confidence in industrial-scale testing of this effect.

Hybrid Energy Flotation™ rows offer optimized collision frequencies via a distribution of energy dissipation values. Experimental work utilizing typical porphyry copper bulk feeds indicates that this approach may offer potential recovery benefits for individual size classes. The application of Hybrid Energy Flotation™ offers the opportunity to optimize metallurgical performance of a single row through ideal management of local energy dissipation in relation to the valuable mineral distribution in the feed. This approach alludes to a shift away from the traditional residence time requirements that constrain flotation circuit design.

References

- ABRAHAMSON, J. 1975. Collision rates of small particles in a vigorously turbulent fluid. *Chemical Engineering Science*, vol. 30, pp. 1371–1379.
- ATA, S., RAHMAN, R.M., AND JAMESON, G.J. 2012. The effect of flotation variables on the recovery of different particle size fractions in the froth and the pulp. *International Journal of Mineral Processing*, vol. 106–109, pp. 70–77.
- BLOOM, F. and HEINDEL, T.J. 2002. On the structure of collision and detachment frequencies in flotation models. *Chemical Engineering Science*, vol. 57, pp. 2467–2473.
- DAI, Z., FORNASIERO, D., and RALSTON, J. 1999. Particle–bubble attachment in mineral flotation. *Journal of Colloid and Interface Science*, vol. 217, no. 1, pp. 70–76.
- DEGLON, D.A. 1998. A hydrodynamic investigation of fine particle flotation in a batch flotation cell. PhD thesis, University of Cape Town, South Africa.
- DEGLON, D.A. 2005. The effect of agitation on the flotation of platinum ores. *Minerals Engineering*, vol. 18, pp. 839–844.
- GOVENDER, D. 2010. Mineral Park – an evaluation into the liquid phase residence time distribution of the Wemco 257m³ rougher-scavenger circuit. *Internal Report*, FLSmidth Salt Lake City Inc.
- GRANO, S. 2006. Effect of impeller rotational speed on the size dependent flotation rate of galena in full scale plant cells. *Minerals Engineering*, vol. 19, pp. 1307–1318.
- JAMESON, G.J. 2010. New directions in flotation machine design. *Minerals Engineering*, vol. 23, pp. 835–841.
- KOH, P.T.L. and SCHWARZ, M.P. 2006. CFD modelling of bubble-particle attachments in flotation cells. *Minerals Engineering*, vol. 19, pp. 619–626.
- KOH, P.T.L. AND SMITH, L.K. 2011. The effect of stirring speed and induction time on flotation. *Minerals Engineering*, vol. 24, pp. 442–448.
- LIEPE, F. and MÖCKEL, H-O. 1976. Untersuchungen zum stoffvereinigen in flüssiger phase. *Chemical Technology*, vol. 30, pp. 205–209.
- RAGAB, S.A. and FAYED, H. 2012. Collision frequency of particles and bubbles suspended in homogeneous isotropic turbulence. AIAA Paper 2012-0310. *AIAA 50th Aerospace Sciences Meeting*, Nashville, TN, 9–12 January 2012.
- SCHUBERT, H. 1989. The role of turbulence in mineral processing unit operations. *Challenges in Mineral Processing*. Sastry, K. and Fuerstenau, M.C. (eds.). SME Inc., Littleton, CO. pp. 272–289.
- SCHUBERT, H. 2008. On the optimization of hydrodynamics in fine particle flotation. *Minerals Engineering*, vol. 21, pp. 930–936.
- SCHUBERT, H. and BISCHOFBERGER, C. 1978. On the hydrodynamics of flotation machines. *International Journal of Mineral Processing*, vol. 5, pp. 131–142.
- SCHULZE, H. 1993. Flotation as a heterocoagulation process: possibilities of calculating the probability of flotation. *Coagulation and Flocculation: Theory and Applications*. Dobiáš, B. (ed.). Marcel Dekker, New York. pp 321–363.
- SHERRELL, I. and YOON, R-H. 2005. Development of a turbulent flotation model. *Proceedings of the Centenary of Flotation Symposium 2005*. The Australian Institute of Mining and Metallurgy, Brisbane. pp 611.
- YOON, R.H. and LUTTRELL, G.H. 1989. The effect of bubble size on fine particle flotation. *Frothing and Flotation*. Laskowski, J. (ed.). (Gordon & Breach, New York. pp. 101–122.
- ZANIN, M., AMETOV, I., GRANO S., ZHOU, L., and SKINNER, W. 2009. A study of mechanisms affecting molybdenite recovery in a bulk copper/molybdenum flotation circuit. *International Journal of Mineral Processing*, vol. 93, pp. 256–266. ◆